

A Large-Scale Benchmark of Cross-Modal Learning for Histology and Gene Expression in Spatial Transcriptomics

Rushin H. Gindra^{1,2*}, Giovanni Palla^{1*}, Mathias Nguyen^{1,2}, Sophia J. Wagner^{1,2},
Manuel Tran^{1,2}, Fabian J Theis^{1,2}, Dieter Saur², Lorin Crawford^{3†}, Tingying Peng^{1,2†}

¹Helmholtz Munich, Germany

²Technical University Munich, Germany

³Microsoft Research, USA

rushin.gindra@helmholtz-munich.de, lcrawford@microsoft.com, tingying.peng@helmholtz-munich.de

Abstract

Spatial transcriptomics enables simultaneous measurement of gene expression and tissue morphology, offering unprecedented insights into cellular organization and disease mechanisms. However, the field lacks comprehensive benchmarks for evaluating multimodal learning methods that leverage both histology images and gene expression data. Here, we present HESCAPE, a large-scale benchmark for cross-modal contrastive pretraining in spatial transcriptomics, built on a curated pan-organ dataset spanning 6 different gene panels and 54 donors. We systematically evaluated state-of-the-art image and gene expression encoders across multiple pre-training strategies and assessed their effectiveness on two downstream tasks: gene mutation classification and gene expression prediction. Our benchmark demonstrates that gene expression encoders are the primary determinant of strong representational alignment, and that gene models pretrained on spatial transcriptomics data outperform both those trained without spatial data and simple baseline approaches. However, downstream task evaluation reveals a striking contradiction: while contrastive pretraining consistently improves gene mutation classification performance, it degrades direct gene expression prediction compared to baseline encoders trained without cross-modal objectives. We identify batch effects as a key factor that interferes with effective cross-modal alignment. Our findings highlight the critical need for batch-robust multimodal learning approaches in spatial transcriptomics. To accelerate progress in this direction, we release HESCAPE, providing standardized datasets, evaluation protocols, and benchmarking tools for the community, at <https://github.com/peng-lab/hescape>

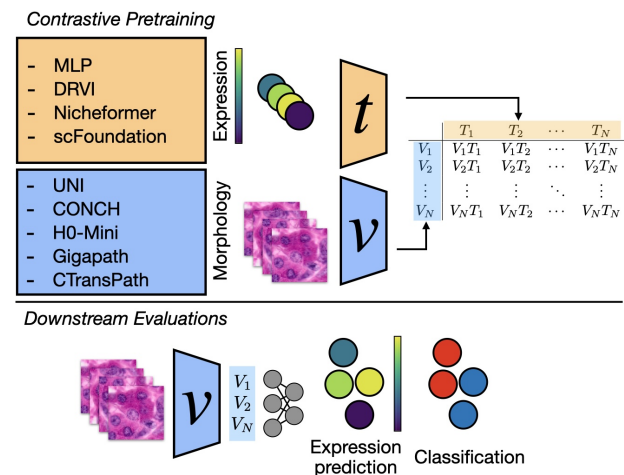


Figure 1. HESCAPE Benchmark: 4 gene expression encoders and 5 image encoders for digital pathology have been fine-tuned with contrastive pretraining, and evaluated in downstream tasks.

1. Introduction

Recent advances in biomedical representation learning have enabled joint modeling of pathology images with reports [29, 46], bulk gene expression [22], and x-ray scans with clinical notes [18], largely driven by large-scale curated datasets and robust training paradigms [12, 30, 47].

The advent of high-throughput spatial omics techniques, including spatial transcriptomics, has opened new avenues for understanding tissue organization at cellular resolution by leveraging joint histological imaging and molecular profiling data [37, 40]. Such techniques have been particularly impactful in cancer pathology research, where routine pathology analysis is paired with whole-transcriptome measurements from the same biospecimen, yielding rich multimodal molecular data with the potential of uncovering new molecular

*Contributed equally

†Corresponding authors

mechanisms and biomarkers [38]. Furthermore, these data can be integrated with legacy data from pathology biobanks.

Pathology foundation models have achieved strong performance across benchmarks [4, 6, 25, 32, 34, 49, 60]. To fully harness the information provided by spatial transcriptomics, we require novel multimodal strategies capable of learning of integrating tissue images with gene expression.

To elucidate this challenge, we curated a large-scale dataset of over $\sim 620k$ patch-level image–gene pairs across multiple organs originating from 6 different 10x Xeniun in-situ panels, collected across 54 patients and 57 individual samples. This dataset enable us to perform a large-scale benchmark of image and gene encoders using contrastive pretraining. Our results demonstrate that dataset-specific pre-training of gene expression encoders has the greatest impact on cross-modality retrieval performance. Additionally, we emphasize the critical importance of addressing batch effects in these encoders. For the gene expression modality specifically, the ability to directly model batch effects provides significant performance improvements in cross-modality retrieval tasks.

We directly evaluate the top-performing methods from contrastive pretraining cross-modality retrieval tasks in real-world downstream applications. Specifically, we assess how contrastive pretraining on spatial transcriptomics datasets impacts performance on two downstream tasks: mutation-specific tumor classification and gene expression prediction from morphology Fig. 1.

Building on these findings, we propose HESCAPE (H&E + Spatial ContrAstive PrEtraining), a framework for contrastive pretraining on spatial transcriptomics data. HESCAPE provides a curated dataset with one-to-one mappings between histological patches and gene expression vectors, along with standardized performance metrics for evaluating new architectures. By making this open benchmark available on Hugging Face, we aim to accelerate the development of robust, clinically applicable spatial omics models that integrate seamlessly with widely adopted imaging encoders. This resource represents a step toward enabling the computer vision community to tackle domain-specific challenges in spatial transcriptomics, thereby advancing both fundamental multi-omics research and translational applications in oncology and beyond.

2. Related work

2.1. Image encoders

The success of large-scale self-supervised learning combined with the availability of large numbers of unlabeled image patches from histology slides initiated the development of domain-specific feature encoders. These models are trained on millions of image patches from hundreds of thousands of patients using contrastive methods such as

MoCov3 (RetCCL [53], CTransPath [52]) or knowledge distillation approaches such as DINO [5] or DINOv2 [36] (Phikon, UNI [6], Virchow [49], H-Optimus-0 [13, 42], Prov-GigaPath [58], Atlas [1]). These pathology-specific encoders provide better and more robust image representations, and enhance critical downstream tasks, such as slide-level biomarker prediction [50] or clinical report generation [46].

2.2. Gene encoders

Single-cell transcriptomics consists of gene expression measurements at single-cell resolution. The data is typically sparse and contains signals reflecting both biological variation (e.g., tissue and cell state variation) and technical variation (e.g., sample preparation, sequencing depth). Variational autoencoders (VAEs) based on multilayer perceptrons (MLPs) such as scVI [28] or DRVI [35] learn a low-dimensional embedding by aiming to reconstruct the gene expression at input. Recently, researchers have developed foundation models for transcriptomics (Geneformer [10], scGPT [8], scFoundation [14], UCE [41], Nicheformer [43], scGPT-spatial [51]) that encode information from tens of millions of cells. While these models show that large-scale pretraining can provide benefit in downstream tasks in single-cell genomics, despite limited model capacity [11], their ability to encode molecular variation in a multimodal representation learning setting has not been tested to date.

2.3. Multi-modal models in histopathology

Combining pre-trained text encoders, image encoders, and gene encoders offers the opportunity to learn richer representations of multimodal patient data such as pathology reports, pathology images, and bulk RNA sequences. Recent models have proposed to align pathology images with text on patch-level (PLIP [17], QUILT-1M [19], CONCH [29], MUSK [56]) or on slide-level (PRISM [45], GigaPath [58], TITAN [12]). Beyond morphological descriptions and clinical reports, pathology slides can be aligned with bulk gene expression (TANGLE [22], FSM [62], THREADS [47], SURVPATH [23]), or immunohistochemistry (MADELEINE [24]). To take a step further, multi-modal integration with 3D spatial-omics has shown promising results (VORTEX [2]).

2.4. Multi-modal in spatial-omics data

Several models have been proposed for integrating the dual modality of spatial omics data [37, 40]. A key challenge is the prediction of gene expression profiles from morphology [3, 15, 44, 61]. This task was recently proposed as a foundational benchmark for multimodal histology and gene expression integration [21]. Other studies suggest pretraining the multimodal representation with contrastive learning [7, 26, 57], showing improved performance for the gene expression prediction task. Nevertheless, a large-scale eval-

Table 1. HESCAPE Dataset characteristics across 10x Xenium gene panels showing number of genes, patches, tissue sections, and samples/donors.

Panel	Genes	Patches	Sections	Donors
5K	5001	178817	7	7
Breast	280	127960	5	5
ImmOnc	380	67050	5	5
Lung	343	56689	20	19
Colon	322	61067	5	3
Multi	377	132040	15	15

uation of multimodal pretraining in spatial omics, which leverages different image and gene expression encoders as well as a large and diverse dataset across various transcriptomic panels, has not been reported. Additionally, the importance of performing multimodal pretraining on spatial-omics data, the correct selection of encoders and its corresponding impact on unimodal downstream task performance for histopathology is yet to be studied.

3. Large-scale Contrastive Pretraining Benchmark For Spatial Transcriptomics

In this work, we devised a large-scale benchmark to test the effectiveness of contrastive pretraining methods for learning multimodal representations of spatial transcriptomics data. In the following section, we describe the datasets, image encoder, and gene expression decoders employed in the benchmark.

3.1. Dataset

We curated a large collection of spatial transcriptomics data from 10x Genomics Xenium consisting of solely human tissues. The HESCAPE collection has 6 datasets, each identified by a subset of samples that share the same gene panels used to measure the samples. To highlight batch effects both across organs and collection sites, as well as to evaluate their effect on multi-modal learning, 3 datasets consist of organ-specific Xenium samples and 3 datasets consist of pan-organ Xenium samples. These samples have been pooled from different sites such as HEST benchmark [21] and other publicly available sources. It consists of a total of 729962 patches (623623 without duplicates). A full description of the dataset curation and preprocessing can be found in Tab. 1 and Supplementary Sec. 7.1.

3.2. Models

We evaluate diverse combinations of image and gene encoder models using contrastive learning across all 6 datasets. To support future development, we open-source the benchmarking code and provide detailed instructions, fostering

collaboration and the adoption of innovative, batch-robust gene encoder practices. The HESCAPE benchmark is designed as a plug-and-play framework, enabling seamless integration and rapid comparison of novel encoders from either modality.

3.2.1. Image encoders

We include five state-of-the-art image encoder models, each trained on a minimum of 15 million pathology patches collected from diverse sources.

CTransPath is a Swin Transformer trained on 15 million patches from 30,000 whole slide images (WSIs) in The Cancer Genome Atlas (TCGA) and Pathology Artificial Intelligence Platform (PAIP) public databases [52].

UNI is a vision transformer (ViT) trained on 100 million patches from more than 100,000 H&E stained WSIs spanning 20 major tissue types using the DINOv2 self-supervised framework based on knowledge distillation [6].

CONCH is a ViT trained using vision-language alignment with CLIP on 1.15 million image-caption pairs curated from PubMed and medical textbooks [29].

Gigapath is a ViT model trained on approximately 1.1 billion pathology patches derived from 170,000 WSIs. Similar to UNI, its patch encoder is trained using the DINOv2 self-supervision framework [58].

H0mini is an 86 million parameters ViT, distilled from 1.1 billion parameters original H-Optimus-0 [42], trained on a proprietary dataset of over 500,000 H&E stained WSIs [13].

3.2.2. Gene encoders

Despite the limited number of dedicated gene encoders for spatial technologies, we evaluate four models that are straightforward to train or fine-tune on spatial datasets. These models have either been developed as foundational models for single-cell or spatial genomics, or they have demonstrated robustness in extracting meaningful embeddings from gene expression data, whether at the single-cell or spatial level.

MLP: A multilayer perceptron (MLP) is a standard baseline for gene expression data. Our implementation uses a simple two-layer MLP with a hidden layer twice the size of the input dimension. This model is trained from scratch alongside the contrastive training on the specific gene expression dataset of interest, providing a straightforward benchmark for gene coding performance.

DRVI: This is an unsupervised VAE-based generative model that learns nonlinear, disentangled representations of single-cell data, designed as an extension to scVI [35]. We pretrain DRVI independently on each gene expression training dataset separately.

scFoundation: A transformer-based foundation model trained on a large collection of single-cell data. Since scFoundation has shown its generalizable feature representations extend to other modalities like bulk RNA-seq data, we apply

the scFoundation model directly without additional spatial fine-tuning [14].

Nicheformer: A transformer-based model based on BERT and adapted to both dissociated single-cell and targeted spatial transcriptomics data (e.g., 10x Xenium), Nicheformer has demonstrated exceptional zero-shot and fine-tuning performance in spatially relevant downstream tasks [43]. We use the frozen nicheformer model in zero-shot settings for our benchmark.

3.3. Pretraining

Our experimental setup is based on a contrastive multi-modal pretraining framework. Each input to the vision encoder is an image patch I_i surrounding a Xenium patch, and the encoder outputs a feature vector $\mathbf{v}_i \in \mathbb{R}^d$, where d is the feature dimension. Each gene encoder processes the corresponding paired expression G_i , with pre-processing steps such as normalization or ranking applied when necessary (based on the encoder requirements). It yields embeddings $\mathbf{g}_i \in \mathbb{R}^d$, where d is the same feature dimension as for the image encoders.

3.3.1. Losses

We leverage the foundational CLIP (Contrastive Language-Image Pre-Training) [39] objective, as well as the newer SigLip (Sigmoid Loss for Language-Image Pre-training) [59] objective.

Specifically, for a minibatch of images and gene expression pairs $\mathcal{B} = \{(I_1, G_1), (I_2, G_2), \dots\}$, the CLIP learning objective for the image-gene expression pair $\mathbf{v}_2 \mathbf{g}_2$ is:

$$L_{\text{CLIP}^{\mathbf{v}2\mathbf{g}}} = -\frac{1}{|\mathcal{B}|} \sum_{i=1}^{|\mathcal{B}|} \log \frac{\exp(\tau \langle \mathbf{v}_i, \mathbf{g}_i \rangle)}{\sum_{j=1}^{|\mathcal{B}|} \exp(\tau \langle \mathbf{v}_i, \mathbf{g}_j \rangle)} \quad (1)$$

where, again, $\mathbf{v}_i \in \mathbb{R}^d$ and $\mathbf{g}_i \in \mathbb{R}^d$ denote the image embeddings and gene embeddings from their respective encoders. The temperature τ is a learnable parameter.

For both losses, the global loss is

$$L_{\text{CLIP}} = \frac{1}{2} [L_{\mathbf{v}2\mathbf{g}} + L_{\mathbf{g}2\mathbf{v}}] \quad (2)$$

where the inner product in $L_{\mathbf{g}2\mathbf{v}}$ is $\langle \mathbf{g}_i, \mathbf{v}_j \rangle$. In this work, we utilize both losses across the pretraining experiments to understand their performance in our data and batch size regime (Supplementary Tab. 10). We leverage the *openclip* implementations in Ilharco et al. [20] for multi-GPU loss computation of CLIP and SigLip.

In the pretraining phase, we experiment with multimodal encoders both frozen and fine-tuned, where we do full fine-tuning for the MLP and DRVI and parameter-efficient fine tuning (PEFT) using LoRA (Low-Rank Adaptation)[16] for all image models, Nicheformer, and scFoundation. Additional description of the experimental configurations are

shown in Sec. 8.2.3. For the final benchmark shown in Tab. 2, we keep all gene encoders frozen except for the MLP baseline, which is trained from scratch alongside the contrastive pretraining.

3.3.2. Metrics

We evaluate the representation quality after image-transcriptomics alignment with Recall@ k for $k = \{1, 5, 10\}$, which measures the proportion of relevant items retrieved within the top k retrieved samples. We report both image-to-gene (I2G) retrieval, where an image query retrieves its corresponding gene-expression profile, and gene-to-image (G2I) retrieval, where a gene-expression query retrieves the matching histological image.

3.4. Downstream evaluations

3.4.1. Gene Mutation Prediction

Driver mutations are a hallmark of cancer. These genetic alterations directly promote the development and growth of cancer cells. They are often associated with tissue morphology (that is, the histological phenotype) and can be identified using deep learning models [50]. In cancer diagnostics, this could eliminate costly and time-consuming molecular tests or genetic assays. For instance, in colorectal cancer (CRC), a mutation in *BRAF* is associated with a poorer prognosis. A vision model that can reliably detect *BRAF* mutations in routine histology images could identify high-risk patients earlier. This would guide the selection of targeted therapies and ultimately improve treatment outcomes. Here, we analyze whether pathology foundation models trained on image data alone are sufficient for biomarker detection and if they can be further improved by aligning gene expression data.

We benchmark multimodal alignment on nine biomarker detection tasks, three biomarkers for CRC: microsatellite instability (MSI), *BRAF*, and *KRAS* status; three biomarkers for breast adenocarcinoma (BRCA): ER, PR, and HER2 status; and three biomarkers for lung adenocarcinoma (LUAD): *EGFR*, *KRAS*, and *TP53* status. All tasks are tested on H&E-stained FFPE WSIs from the respective cohorts of TCGA [27, 54].

3.4.2. HEST Benchmark

Fine-tuned image encoders are evaluated on the HEST benchmark [21] by regressing patch-level gene expression from image patches. The benchmark comprises nine tasks that span various tissue types and cancer subtypes from both 10x xenium and visium datasets. Each task predicts the expression of the top 50 most variable genes from 224×224 pixel histology patches $112 \mu\text{m} \times 112 \mu\text{m}$ at 20x magnification. The features extracted at the patch level are then passed to a ridge regression model for gene expression prediction.

To ensure a fair comparison and avoid data leakage, we maintained the identical train/test splits used in the pretraining phase, which vary slightly from the HEST benchmark.

Further descriptions on dataset creation and train/test splits have been reported in the Supplementary Sec. 7.1.

Here, we assess whether HESCAPE-aligned image encoders trained with spatial transcriptomics yield better expression prediction performance. We report Pearson’s correlation coefficient (PCC) and mean squared error (MSE) between predicted and measured gene expression, averaged across genes and cross-validation folds (patient-level splits).

4. Results

4.1. Contrastive Pretraining

Our large-scale pretraining benchmark demonstrates that the gene encoder DRVI emerges as the key determinant of performance improvement across all tissue panels and both image-to-gene (I2G) and gene-to-image (G2I) metrics (Tab. 2 and Supplementary Tab. 7–Tab. 8). Notably, DRVI paired with the image encoders Gigapath, H0mini, and UNI consistently achieves the top-performing Recall@5 scores across datasets. This superior performance is likely attributable to DRVI’s pretraining on the gene expression modality of the training set and its capability to handle batch effects effectively.

When examining pre-trained gene foundation models, our findings reveal that despite their pretraining on large-scale datasets, they cannot surpass VAE-based models like DRVI pretrained on the dataset of interest. However, despite the training of MLP baselines on the dataset of interest, foundation models do demonstrate substantial improvements over them, with performance gains ranging from approximately 2-5x across different tissue types. Among the foundation models in our benchmark, Nicheformer consistently outperforms scFoundation across all evaluated datasets, highlighting the advantage of pretraining on spatial transcriptomics data compared to models trained exclusively on single-cell genomics data.

The results also reveal significant heterogeneity in performance across tissue types, with lung tissue showing the highest overall performance (Recall@5 up to 0.709 for Gigapath-DRVI G2I) and the 5K dataset showing the most challenging retrieval task. Interestingly, while the I2G and G2I tasks generally show comparable performance patterns, some tissue-specific variations emerge, particularly in breast and lung datasets, where certain models show slightly asymmetric performance between the two retrieval directions.

Additionally, we perform several ablation studies to observe contributing factors for optimal pretraining. From these ablations, we observe, an optimal combination of MLP projection, CLIP loss with fine-tunable image and gene encoders performs well across all spatial datasets. However, limited computational resources require us to perform locked gene-image tuning to improve the image encoders. The ablations have been reported in Sec. 8.2 and Supplementary Tab. 9, Tab. 10, and Tab. 11.

4.2. Gene Mutation Prediction

We tested whether contrastive pretraining with gene expression profiles provides improvements on whole-slide image (WSI) level classification tasks. To test how gene-panel specific pretraining affects the downstream performance across various organs, we choose our top 2 performing models Gigapath-DRVI and UNI-DRVI trained on the Human Multi-Tissue Panel. Additionally, to show how gene-encoder selection can affect downstream tasks, for the Human 5K Panel, we selected Gigapath-DRVI as our top model and UNI-Nicheformer as our sub-optimal model. The Human 5K Panel and the Human Multi-Tissue Panel were used as the common dataset for training to show that performance gains in gene mutation prediction task are not specific to certain organ datasets. We conducted downstream evaluations on mutation prediction for three biomarkers for CRC, three for BRCA, and three for LUAD (Sec. 3.4.1).

The results in Tab. 3 reveal a nuanced pattern regarding the benefits of contrastive pretraining with gene expression encoders. For MSI prediction, Gigapath-DRVI achieves the best performance in F1 score (0.558), outperforming the baseline Gigapath model (0.484), representing a 15.3% improvement. Similarly, for *BRAF* prediction, UNI-DRVI (0.395) outperforms the respective baseline model (0.325) by 21.5% and the best baseline model Gigapath (0.381) by 2.6%. However, for *KRAS* prediction in CRC, both baseline models, UNI (0.495) and Gigapath (0.491), outperform their gene expression-pretrained counterparts, Gigapath-DRVI (0.474) and UNI-DRVI (0.364).

Similarly, biomarker prediction in BRCA demonstrates a comparable pattern of performance (Tab. 4). For ER status prediction, Gigapath-DRVI achieves the highest F1 score of 0.898, representing a slight improvement over the baseline Gigapath (0.890), consistent with the UNI variants. For PR status prediction, Gigapath-DRVI again shows the best performance with an F1 score of 0.829, outperforming both baseline models, Gigapath (0.811) and UNI (0.807). However, for HER2 status prediction, the baseline models demonstrate superior performance, with UNI achieving the highest F1 score of 0.439, compared to the gene expression-pretrained models, Gigapath-DRVI (0.401) and UNI-DRVI (0.368).

Finally, WSI gene mutation prediction in LUAD results in the same biomarker-specific pattern, though with more pronounced improvements depending on the vision backbone (Tab. 5). For two out of three biomarkers, pretraining with gene expression encoders demonstrates substantial performance gains. Most notably, for *EGFR* prediction, Gigapath-DRVI achieves an F1 score of 0.299, representing a dramatic 100% improvement over the baseline Gigapath (0.149). Similarly, for *KRAS* prediction, Gigapath-DRVI from the 5K panel achieves the best performance with an F1 score of 0.433, outperforming the baseline Gigapath (0.367).

Table 2. Complete Test Recall@5 Results for both Image-to-Gene (I2G) and Gene-to-Image (G2I) tasks across different tissue panels. Experiments with “—” indicate out of memory issues during training. Best results are in **bold**, second-best are underlined.

Model	5K		Multi		ImmOnc		Colon		Breast		Lung	
	I2G	G2I										
MLP-CTransPath	0.103	0.106	0.138	0.098	0.110	0.094	0.098	0.122	0.116	0.117	0.103	0.126
MLP-CONCH	0.228	0.228	0.241	0.178	0.187	0.130	0.300	0.258	0.383	0.260	0.443	0.418
MLP-Gigapath	0.257	0.257	0.297	0.215	0.179	0.132	0.313	0.297	0.390	0.288	0.510	0.493
MLP-H0mini	0.235	0.235	0.209	0.153	0.173	0.119	0.296	0.291	0.309	0.235	0.358	0.336
MLP-UNI	0.247	0.246	0.255	0.171	0.243	0.130	0.320	0.317	0.346	0.248	0.493	0.493
scFoundation-CTransPath	—	—	—	—	0.119	0.126	0.105	0.098	0.138	0.122	0.125	0.121
scFoundation-CONCH	—	—	—	—	0.219	0.177	0.287	0.262	0.331	0.309	0.503	0.458
scFoundation-Gigapath	—	—	—	—	0.251	0.207	0.294	0.249	0.348	0.365	0.590	0.543
scFoundation-H0mini	—	—	—	—	0.206	0.171	0.315	0.272	0.388	0.377	0.427	0.345
scFoundation-UNI	—	—	—	—	0.236	0.173	0.297	0.244	0.358	0.351	0.543	0.479
Nicheformer-CTransPath	0.105	0.115	0.126	0.117	0.127	0.127	0.092	0.106	0.110	0.126	0.122	0.138
Nicheformer-CONCH	0.237	0.274	0.258	0.286	0.224	0.247	0.267	0.253	0.366	0.410	0.412	0.496
Nicheformer-Gigapath	0.241	0.255	0.274	0.285	0.247	0.267	0.261	0.269	0.414	0.447	0.473	0.554
Nicheformer-H0mini	0.243	0.273	0.261	0.277	0.212	0.215	0.290	0.278	0.418	0.451	0.424	0.498
Nicheformer-UNI	0.259	0.291	0.269	0.288	0.243	0.261	0.252	0.250	0.416	0.442	0.449	0.538
DRV1-CTransPath	0.106	0.116	0.116	0.147	0.138	0.135	0.111	0.123	0.162	0.144	0.143	0.163
DRV1-CONCH	0.266	0.316	0.298	0.363	0.300	0.290	0.356	0.362	0.397	0.397	0.539	0.597
DRV1-Gigapath	<u>0.315</u>	0.359	<u>0.322</u>	0.417	0.344	<u>0.334</u>	0.388	0.394	<u>0.461</u>	<u>0.436</u>	0.649	0.709
DRV1-H0mini	0.299	0.321	0.271	0.342	0.287	0.267	0.412	<u>0.397</u>	0.465	0.461	0.562	0.612
DRV1-UNI	0.322	0.341	<u>0.312</u>	<u>0.396</u>	0.326	0.318	0.404	0.401	0.450	0.436	<u>0.610</u>	<u>0.678</u>

Table 3. Performance comparison of different encoders on CRC classification tasks. Results show F1 scores (mean(std)) for MSI, *BRAF*, and *KRAS* prediction tasks. Best results are in **bold**, second-best are underlined.

Encoder	MSI	BRAF	KRAS
Gigapath	0.484(0.059)	0.381(0.108)	0.491(0.106)
UNI	0.472(0.099)	0.325(0.137)	0.495(0.088)
Human Multi-Tissue Panel			
Gigapath-DRV1	0.558(0.091)	0.394(0.104)	0.474(0.097)
UNI-DRV1	0.465(0.098)	0.395(0.076)	0.364(0.210)
Human 5K Panel			
Gigapath-DRV1	0.473(0.093)	0.353(0.041)	0.421(0.098)
UNI-Nicheformer	0.416(0.032)	0.338(0.092)	0.419(0.156)

by 18%. However, for *TP53* prediction, there isn’t a substantial improvement of the trained models over the baseline Gigapath which has an F1 score of 0.705, while both gene expression-pretrained variants score similarly with high variance across different training folds, Gigapath-DRV1 (0.695) and UNI-DRV1 (0.649). This pattern could be observed due to variations in self-supervised training data used for UNI and Gigapath baselines. The pattern also reinforces the biomarker-specific nature of the benefits observed across all three cancer types.

It should be noted that in the case of LUAD WSI gene

Table 4. Performance comparison of different encoders on BRCA classification tasks. Results show F1 scores (mean(std)) for ER, PR, and HER2 prediction tasks. Best results are in **bold**, second-best are underlined.

Encoder	ER	PR	HER2
Gigapath	0.890(0.022)	0.811(0.019)	0.388(0.053)
UNI	0.857(0.017)	0.807(0.038)	0.439(0.021)
Human Multi-Tissue Panel			
Gigapath-DRV1	0.898(0.028)	0.829(0.039)	0.401(0.042)
UNI-DRV1	0.887(0.043)	0.817(0.022)	0.368(0.058)
Human 5K Panel			
Gigapath-DRV1	0.872(0.018)	0.799(0.026)	0.407(0.023)
UNI-Nicheformer	0.858(0.022)	0.808(0.030)	0.433(0.023)

mutation prediction, we only had one sample of LUAD measured with Xenium technologies for each of the two gene panels under consideration (Human 5K Panel and Human Multi-Tissue Panel). Hence, this represents pretraining in a pan-cancer setting rather than lung-specific pretraining, which may explain some of the performance variations observed compared to the more tissue-specific pretraining scenarios in CRC and BRCA analyses.

An important limitation of this analysis is that the expression profiles of the target genes associated with the genomic abnormalities were not available in our Xenium datasets

Table 5. Performance comparison of different encoders on LUAD classification tasks. Results show F1 scores (mean(std)) for *EGFR*, *KRAS*, and *TP53* prediction tasks. Best results are in **bold**, second-best are underlined.

Encoder	<i>EGFR</i>	<i>KRAS</i>	<i>TP53</i>
Gigapath	0.149(0.0797)	0.367(0.1437)	0.705(0.0567)
UNI	0.349(0.070)	0.382(0.095)	0.693(0.057)
Human Multi-Tissue Panel			
Gigapath-DRV1	0.299(0.0432)	0.371(0.0970)	0.668(0.0662)
UNI-DRV1	0.329(0.0610)	0.379(0.0839)	0.649(0.0769)
Human 5K Panel			
Gigapath-DRV1	0.328(0.0383)	0.433(0.0791)	0.695(0.0656)
UNI-Nicheformer	0.301(0.0437)	0.387(0.1156)	0.658(0.0581)

used for pretraining. For instance, when predicting *TP53* mutations, the actual *TP53* gene expression values were not measured in the spatial transcriptomics samples. Consequently, the models could only leverage latent correlation structures between the measured genes in the spatial transcriptomics data and the genomic abnormalities of interest, rather than direct gene-to-mutation associations.

This constraint may explain some of the observed variability in predictive performance across different biomarkers. Mutations in genes with stronger co-expression networks or clearer downstream effects on the measured gene panel are more likely to be predicted accurately through correlated expression patterns. In contrast, mutations in genes with weaker or more complex regulatory relationships to the measured genes might be harder to detect through proxy gene expression patterns. For instance, in BRCA, ESR1 gene is tightly linked to the ER receptor status, PGR to PR status and ERBB2 to HER2 receptor status. All three of these genes are included in the Multi-tissue and Prime 5K gene panels.

In summary, this analysis demonstrates that while integrating molecular knowledge into vision models can improve WSI mutation prediction for certain biomarkers, the effectiveness is highly biomarker-specific. The success appears to depend on both the strength of underlying biological relationships between histological features and gene expression variation, as well as the presence of measurable proxy signals within the available gene expression data that correlate with the target genomic abnormalities.

4.3. Gene Expression Prediction

Next, we investigated whether contrastive pretraining improves the downstream task of predicting gene expression directly from histological images. Based on the superior retrieval performance demonstrated in Tab. 2, we selected the top-performing pretrained multimodal encoders and evaluated their image encoders on gene expression prediction using a ridge regression head as performed in the HEST gene expression prediction benchmark [21]. To ensure a fair

comparison and avoid data leakage, we maintained the identical train/test splits used in the pretraining phase. The gene expression prediction performance, evaluated using Pearson correlation coefficient (PCC) and mean squared error (MSE), is reported in Tab. 6.

Surprisingly, the results in Tab. 6 reveal a counterintuitive pattern: contrastive pretraining with gene expression encoders does not consistently improve direct gene expression prediction from histological images. Across all four datasets, the baseline image encoders (without gene expression pretraining) generally achieve superior or comparable performance compared to their pretrained counterparts. For instance, in the 5K dataset, the baseline Gigapath model achieves the highest PCC of both image encoders pre-trained on the Multi and 5K variants. This pattern is consistent across other datasets, where the baseline H0mini achieves the best performance in the ImmOnc, Breast, and Lung datasets.

This negative result is counterintuitive, given that cross-modal pretraining should, in principle, improve the prediction of one modality from the other. We propose two possible explanations for this discrepancy from our initial hypothesis.

First, the strong batch effects present in the gene expression modality may skew the image encoder’s learned representations, causing it to prioritize batch-specific patterns over generalizable biological features, thereby reducing performance on the test set. Second, we hypothesize that the alignment process itself may be detrimental to the image encoder’s representational quality. During contrastive pre-training, the image encoder may be forced to discard rich morphological and spatial information that is crucial for gene expression prediction but not necessary for the contrastive task.

To support this hypothesis, we present an analysis on evaluating the magnitude of batch effects in Figure 2 and Supplementary Sec. 8.3, leveraging the Silhouette Batch score from scib [31].

Datasets with better batch integration (higher Silhouette Batch scores) consistently achieve superior cross-modal retrieval performance, suggesting that technical artifacts in the gene expression modality can substantially hinder the learning of meaningful cross-modal representations.

This potentially creates a trade-off between representation alignment and representation quality: while the pretrained encoder learns features that are better aligned with gene expression patterns, these aligned features may be less informative for the downstream prediction task compared to the richer, more generalizable features learned by the baseline encoder. In summary, the biological correlation between histological features and gene expression may be weaker than initially assumed or may be strongly affected by experimental noise such as batch effects. This creates a challenging environment for cross-modal pretraining, where

Table 6. Gene Expression Prediction Task as given by HEST benchmark. Best results are in **bold**.

Model	5K		ImmOnc		Breast		Lung	
	PCC	MSE	PCC	MSE	PCC	MSE	PCC	MSE
H0mini	0.321(0.022)	2.726(0.831)	0.571(0.026)	6.198(0.137)	0.639(0.050)	15.237(3.962)	0.628(0.013)	10.466(0.109)
Gigapath	0.338(0.021)	2.408(0.877)	0.546(0.030)	6.167(0.210)	0.607(0.049)	15.753(5.160)	0.609(0.024)	10.604(0.406)
UNI	0.319(0.031)	2.535(1.164)	0.546(0.020)	5.984(0.163)	0.605(0.023)	14.428(5.404)	0.607(0.019)	10.705(0.593)
Human Multi-Tissue Panel								
DRVI-H0mini	0.247(0.048)	2.713(0.626)	0.476(0.038)	6.204(0.212)	0.520(0.002)	10.849(3.173)	0.479(0.005)	11.152(1.008)
DRVI-Gigapath	0.277(0.020)	2.461(0.712)	0.479(0.028)	6.011(0.075)	0.560(0.026)	10.600(3.593)	0.549(0.010)	10.984(1.182)
DRVI-UNI	0.231(0.062)	3.126(0.499)	0.487(0.028)	5.986(0.134)	0.568(0.048)	10.362(3.661)	0.548(0.007)	10.467(0.217)
Human 5K Panel								
DRVI-H0mini	0.218(0.032)	2.895(0.920)	0.493(0.038)	5.974(0.391)	0.519(0.039)	11.260(3.737)	0.501(0.005)	11.339(0.757)
DRVI-Gigapath	0.232(0.018)	2.665(0.884)	0.530(0.039)	6.230(0.219)	0.571(0.062)	11.228(4.492)	0.563(0.009)	10.485(1.225)
DRVI-UNI	0.264(0.035)	2.661(0.671)	0.495(0.023)	6.280(0.269)	0.592(0.065)	11.904(5.408)	0.543(0.000)	10.845(1.146)

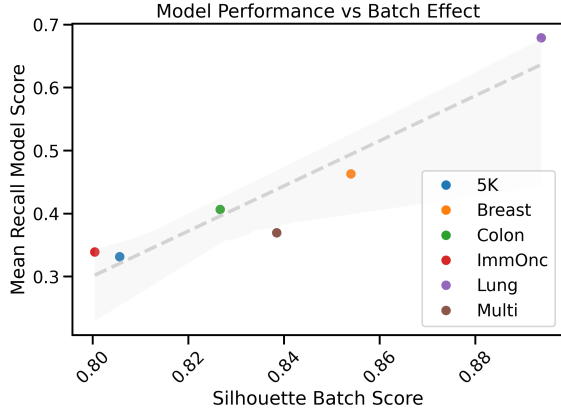


Figure 2. Silhouette Batch score against Mean Recall@5 for Gigapath-DRVI encoder models. Interestingly, there is a clear trend between the cross-modal retrieval task and the magnitude of batch effect in the train/val/test split.

strong domain-specific effects in each modality can interfere with learning meaningful cross-modal relationships. Our findings suggest that future work should focus on developing multimodal encoders that explicitly account for and mitigate domain-specific effects within each modality. Such approaches could potentially achieve greater robustness to batch effects while still leveraging the benefits of contrastive pretraining with spatial transcriptomics data. This would involve disentangling biological signal from technical noise either in an additional pretraining stage before cross-modal alignment, or online during contrastive pretraining [9], potentially leading to more effective and generalizable multimodal representations.

5. Conclusion

In this work, we conducted a large-scale benchmark of contrastive pretraining encoders for cross-modal alignment of morphology and gene expression modalities in histopathology.

We demonstrated improved performance on cross-modal retrieval tasks when encoders were pretrained on the dataset of interest and capable of handling batch effects appropriately. Among the foundation models tested, those directly pretrained on spatial transcriptomics data showed superior performance, highlighting the importance of including spatial transcriptomics data in the pretraining corpus for foundational single-cell genomics representations.

Furthermore, we evaluated pretrained image encoders on two downstream tasks: gene mutation classification and gene expression prediction for specific biomarkers. For mutation classification, cross-modally pretrained image encoders showed convincing improvements in performance. However, for gene expression prediction, the results were mixed, with baseline encoders often outperforming their cross-modally pretrained counterparts. This finding conflicts with findings in the literature where pretraining with gene expression appears to always improve image-to-gene expression prediction tasks [7, 26, 57].

We hypothesize that these results are driven by strong domain-specific effects in the gene expression modality, particularly batch effects that may interfere with the learning of generalizable cross-modal representations. Our analysis provides evidence for such effects and suggests that further investigation is required to directly address domain-specific effects towards learning robust and transferable multimodal representations of morphology and gene expression. Such advances would have a significant translational impact in digital pathology and patient stratification applications.

6. Acknowledgments

R.H.G., G.P, S.J.W., M.T were supported by the Helmholtz Association under the joint research school ‘‘Munich School for Data Science - MUDS’’. S.J.W. was supported by Add-on Fellowship of the Joachim Herz Foundation. The compute resources for the project were supported by de.NBI Cloud within the German Network for Bioinformatics Infrastructure.

ture (de.NBI), ELIXIR-DE (Forschungszentrum Jülich) and Helmholtz Association's Initiative and Networking Fund on the HAICORE@FZJ partition.

References

- [1] Maximilian Alber, Stephan Tietz, Jonas Dippel, Timo Milbich, Timothée Lesort, Panos Korfiatis, Moritz Krügener, Beatriz Perez Cancer, Neelay Shah, Alexander Möllers, Philipp Seegerer, Alexandra Carpen-Amarie, Kai Standvoss, Gabriel Dernbach, Edwin de Jong, Simon Schallenberg, Andreas Kunft, Helmut Hoffer von Ankershoffen, Gavin Schaeferle, Patrick Duffy, Matt Redlon, Philipp Jurmeister, David Horst, Lukas Ruff, Klaus-Robert Müller, Frederick Klauschen, and Andrew Norgan. Atlas: A novel pathology foundation model by mayo clinic, charité, and aignostics, 2025. [2](#)
- [2] Cristina Almagro-Pérez, Andrew H. Song, Luca Weishaupt, Ahrong Kim, Guillaume Jaume, Drew F. K. Williamson, Konstantin Hemker, Ming Y. Lu, Kritika Singh, Bowen Chen, Long Phi Le, Alexander S. Baras, Sizun Jiang, Ali Bashashati, Jonathan T. C. Liu, and Faisal Mahmood. Ai-driven 3d spatial transcriptomics, 2025. [2](#)
- [3] Ludvig Bergensträhle, Bryan He, Joseph Bergensträhle, Xesús Abalo, Reza Mirzazadeh, Kim Thrane, Andrew L Ji, Alma Andersson, Ludvig Larsson, Nathalie Stakenborg, Guy Boeckxstaens, Paul Khavari, James Zou, Joakim Lundeberg, and Jonas Maaskola. Super-resolved spatial transcriptomics by deep data fusion. *Nat. Biotechnol.*, 2021. [2](#)
- [4] Gabriele Campanella, Shengjia Chen, Manbir Singh, Ruchika Verma, Silke Muehlstedt, Jennifer Zeng, Aryeh Stock, Matt Croken, Brandon Veremis, Abdulkadir Elmas, Ivan Shujski, Noora Neittaanmäki, Kuan-lin Huang, Ricky Kwan, Jane Houldsworth, Adam J. Schoenfeld, and Chad Vanderbilt. A clinical benchmark of public self-supervised pathology foundation models. *Nature Communications*, 16(1):3640, 2025. [2](#)
- [5] Mathilde Caron, Hugo Touvron, Ishan Misra, Hervé Jégou, Julien Mairal, Piotr Bojanowski, and Armand Joulin. Emerging properties in self-supervised vision transformers. In *Proceedings of the IEEE/CVF international conference on computer vision*, pages 9650–9660, 2021. [2](#)
- [6] Richard J Chen, Tong Ding, Ming Y Lu, Drew FK Williamson, Guillaume Jaume, Andrew H Song, Bowen Chen, Andrew Zhang, Daniel Shao, Muhammad Shaban, et al. Towards a general-purpose foundation model for computational pathology. *Nature Medicine*, 30(3):850–862, 2024. [2, 3](#)
- [7] Weiqing Chen, Pengzhi Zhang, Tu N. Tran, Yiwei Xiao, Shengyu Li, Vrutant V. Shah, Hao Cheng, Kristopher W. Brannan, Keith Youker, Li Lai, Longhou Fang, Yu Yang, Nhat-Tu Le, Jun-ichi Abe, Shu-Hsia Chen, Qin Ma, Ken Chen, Qianqian Song, John P. Cooke, and Guangyu Wang. A visual–omics foundation model to bridge histopathology with spatial transcriptomics. *Nature Methods*, 2025. [2, 8](#)
- [8] Haotian Cui, Chloe Wang, Hassaan Maan, Kuan Pang, Fengning Luo, Nan Duan, and Bo Wang. scgpt: toward building a foundation model for single-cell multi-omics using generative ai. *Nature Methods*, 21(8):1470–1480, 2024. [2](#)
- [9] Quan Cui, Boyan Zhou, Yu Guo, Weidong Yin, Hao Wu, Osamu Yoshie, and Yubo Chen. Contrastive vision-language pre-training with limited resources. *arXiv [cs.CV]*, 2021. [8](#)
- [10] Zhanbei Cui, Tongda Xu, Jia Wang, Yu Liao, and Yan Wang. Geneformer: Learned gene compression using transformer-based context modeling. In *ICASSP 2024-2024 IEEE International Conference on Acoustics, Speech and Signal Processing (ICASSP)*, pages 8035–8039. IEEE, 2024. [2](#)
- [11] Alan DenAdel, Madeline Hughes, Akshaya Thoutam, Anay Gupta, Andrew W. Navia, Nicolo Fusi, Srivatsan Raghavan, Peter S. Winter, Ava P. Amini, and Lorin Crawford. Evaluating the role of pre-training dataset size and diversity on single-cell foundation model performance. *bioRxiv*, 2024. [2](#)
- [12] Tong Ding, Sophia J Wagner, Andrew H Song, Richard J Chen, Ming Y Lu, Andrew Zhang, Anurag J Vaidya, Guillaume Jaume, Muhammad Shaban, Ahrong Kim, et al. Multimodal whole slide foundation model for pathology. *arXiv preprint arXiv:2411.19666*, 2024. [1, 2](#)
- [13] Alexandre Filion, Nicolas Dop, Oussama Tchita, Auriane Riou, Rémy Dubois, Thomas Peeters, Daria Valter, Marin Scalbert, Charlie Saillard, Geneviève Robin, and Antoine Olivier. Distilling foundation models for robust and efficient models in digital pathology, 2025. [2, 3](#)
- [14] Minsheng Hao, Jing Gong, Xin Zeng, Chiming Liu, Yucheng Guo, Xingyi Cheng, Taifeng Wang, Jianzhu Ma, Xuegong Zhang, and Le Song. Large-scale foundation model on single-cell transcriptomics. *Nature methods*, 21(8):1481–1491, 2024. [2, 4](#)
- [15] Bryan He, Ludvig Bergensträhle, Linnea Stenbeck, Abubakar Abid, Alma Andersson, Åke Borg, Jonas Maaskola, Joakim Lundeberg, and James Zou. Integrating spatial gene expression and breast tumour morphology via deep learning. *Nat. Biomed. Eng.*, 4(8):827–834, 2020. [2](#)
- [16] Edward J. Hu, Yelong Shen, Phillip Wallis, Zeyuan Allen-Zhu, Yuanzhi Li, Shean Wang, Lu Wang, and Weizhu Chen. Lora: Low-rank adaptation of large language models, 2021. [4, 14](#)
- [17] Zhi Huang, Federico Bianchi, Mert Yuksekogun, Thomas J. Montine, and James Zou. A visual–language foundation model for pathology image analysis using medical twitter. *Nature Medicine*, 29(9):2307–2316, 2023. [2](#)
- [18] Stephanie L. Hyland, Shruthi Bannur, Kenza Bouzid, Daniel C. Castro, Mercy Ranjit, Anton Schwaighofer, Fernando Pérez-García, Valentina Salvatelli, Shaury Srivastav, Anja Thieme, Noel Codella, Matthew P. Lungren, Maria Teodora Wetscherek, Ozan Oktay, and Javier Alvarez-Valle. Maira-1: A specialised large multimodal model for radiology report generation, 2024. [1](#)
- [19] Wisdom Oluchi Ikezogwo, Mehmet Saygin Seyfoglu, Fatehme Ghezloo, Dylan Stefan Chan Geva, Fatwir Sheikh Mohammed, Pavan Kumar Anand, Ranjay Krishna, and Linda Shapiro. Quilt-1m: One million image-text pairs for histopathology. *arXiv preprint arXiv:2306.11207*, 2023. [2](#)
- [20] Gabriel Ilharco, Mitchell Wortsman, Ross Wightman, Cade Gordon, Nicholas Carlini, Rohan Taori, Achal Dave, Vaishal Shankar, Hongseok Namkoong, John Miller, Hannaneh Hajishirzi, Ali Farhadi, and Ludwig Schmidt. Openclip, 2021. [4](#)

[21] Guillaume Jaume, Paul Doucet, Andrew Song, Ming Yang Lu, Cristina Almagro Pérez, Sophia Wagner, Anurag Vaidya, Richard Chen, Drew Williamson, Ahrong Kim, et al. Hest-1k: A dataset for spatial transcriptomics and histology image analysis. *Advances in Neural Information Processing Systems*, 37:53798–53833, 2024. [2](#), [3](#), [4](#), [7](#)

[22] Guillaume Jaume, Lukas Oldenburg, Anurag Vaidya, Richard J. Chen, Drew F. K. Williamson, Thomas Peeters, Andrew H. Song, and Faisal Mahmood. Transcriptomics-guided slide representation learning in computational pathology, 2024. [1](#), [2](#)

[23] Guillaume Jaume, Anurag Vaidya, Richard Chen, Drew Williamson, Paul Liang, and Faisal Mahmood. Modeling dense multimodal interactions between biological pathways and histology for survival prediction, 2024. [2](#)

[24] Guillaume Jaume, Anurag Vaidya, Andrew Zhang, Andrew H. Song, Richard J. Chen, Sharifa Sahai, Dandan Mo, Emilio Madrigal, Long Phi Le, and Faisal Mahmood. Multistain pre-training for slide representation learning in pathology, 2024. [2](#)

[25] Yu-Chia Lan, Martin Strauch, Pourya Pilva, Nikolas E. J. Schmitz, Alireza Vafaei Sadr, Leon Niggemeier, Huong Quynh Nguyen, David L. Hölscher, Tri Q. Nguyen, Jesper Kers, Roman D. Bülow, and Peter Boor. Ecologically sustainable benchmarking of ai models for histopathology. *npj Digital Medicine*, 7(1):378, 2024. [2](#)

[26] Yongju Lee, Xinhao Liu, Minsheng Hao, Tianyu Liu, and Aviv Regev. Pathomclip: Connecting tumor histology with spatial gene expression via locally enhanced contrastive learning of pathology and single-cell foundation model. *bioRxiv*, 2024. [2](#), [8](#)

[27] Jianfang Liu, Tara Lichtenberg, Katherine A Hoadley, Laila M Poisson, Alexander J Lazar, Andrew D Cherniack, Albert J Kovatich, Christopher C Benz, Douglas A Levine, Adrian V Lee, et al. An integrated tcga pan-cancer clinical data resource to drive high-quality survival outcome analytics. *Cell*, 173(2): 400–416, 2018. [4](#)

[28] Romain Lopez, Jeffrey Regier, Michael B Cole, Michael I Jordan, and Nir Yosef. Deep generative modeling for single-cell transcriptomics. *Nature methods*, 15(12):1053–1058, 2018. [2](#)

[29] Ming Y Lu, Bowen Chen, Drew FK Williamson, Richard J Chen, Ivy Liang, Tong Ding, Guillaume Jaume, Igor Odintsov, Long Phi Le, Georg Gerber, et al. A visual-language foundation model for computational pathology. *Nature Medicine*, 30 (3):863–874, 2024. [1](#), [2](#), [3](#)

[30] Ming Y Lu, Bowen Chen, Drew FK Williamson, Richard J Chen, Melissa Zhao, Aaron K Chow, Kenji Ikemura, Ahrong Kim, Dimitra Pouli, Ankush Patel, et al. A multimodal generative ai copilot for human pathology. *Nature*, 634(8033): 466–473, 2024. [1](#)

[31] Malte D Luecken, M Büttner, K Chaichoompu, A Danese, M Interlandi, M F Mueller, D C Strobl, L Zappia, M Dugas, M Colomé-Tatché, and Fabian J Theis. Benchmarking atlas-level data integration in single-cell genomics. *Nat. Methods*, 19(1):41–50, 2022. [7](#), [14](#)

[32] Jiabo Ma, Yingxue Xu, Fengtao Zhou, Yihui Wang, Cheng Jin, Zhengrui Guo, Jianfeng Wu, On Ki Tang, Huajun Zhou, Xi Wang, Luyang Luo, Zhengyu Zhang, Du Cai, Zizhao Gao, Wei Wang, Yueping Liu, Jiankun He, Jing Cui, Zhenhui Li, Jing Zhang, Feng Gao, Xiuming Zhang, Li Liang, Ronald Cheong Kin Chan, Zhe Wang, and Hao Chen. Pathbench: A comprehensive comparison benchmark for pathology foundation models towards precision oncology, 2025. [2](#)

[33] Luca Marconato, Giovanni Palla, Kevin A. Yamauchi, Isaac Virshup, Elyas Heidari, Tim Treis, Wouter-Michiel Vierdag, Marcella Toth, Sonja Stockhaus, Rahul B. Shrestha, Benjamin Rombaut, Lotte Pollaris, Laurens Lehner, Harald Vöhringer, Ilia Kats, Yvan Saeys, Sinem K. Saka, Wolfgang Huber, Moritz Gerstung, Josh Moore, Fabian J. Theis, and Oliver Stegle. Spatialdata: an open and universal data framework for spatial omics. *Nature Methods*, 22(1):58–62, 2025. [12](#)

[34] Pablo Meseguer, Rocío del Amor, and Valery Naranjo. Benchmarking histopathology foundation models in a multi-center dataset for skin cancer subtyping, 2025. [2](#)

[35] Amir Ali Moinfar and Fabian J Theis. Unsupervised deep disentangled representation of single-cell omics. *bioRxiv*, pages 2024–11, 2024. [2](#), [3](#)

[36] Maxime Oquab, Timothée Darcet, Théo Moutakanni, Huy Vo, Marc Szafraniec, Vasil Khalidov, Pierre Fernandez, Daniel Haziza, Francisco Massa, Alaeldin El-Nouby, et al. Dinov2: Learning robust visual features without supervision. *arXiv preprint arXiv:2304.07193*, 2023. [2](#)

[37] Giovanni Palla, David S Fischer, Aviv Regev, and Fabian J Theis. Spatial components of molecular tissue biology. *Nat. Biotechnol.*, 40(3):308–318, 2022. [1](#), [2](#)

[38] Young Min Park and De-Chen Lin. Moving closer towards a comprehensive view of tumor biology and microarchitecture using spatial transcriptomics. *Nature Communications*, 14(1), 2023. [2](#)

[39] Alec Radford, Jong Wook Kim, Chris Hallacy, Aditya Ramesh, Gabriel Goh, Sandhini Agarwal, Girish Sastry, Amanda Askell, Pamela Mishkin, Jack Clark, Gretchen Krueger, and Ilya Sutskever. Learning transferable visual models from natural language supervision. 2021. [4](#)

[40] Anjali Rao, Dalia Barkley, Gustavo S França, and Itai Yanai. Exploring tissue architecture using spatial transcriptomics. *Nature*, 596(7871):211–220, 2021. [1](#), [2](#)

[41] Yanay Rosen, Yusuf Roohani, Ayush Agarwal, Leon Samotorčan, Tabula Sapiens Consortium, Stephen R Quake, and Jure Leskovec. Universal cell embeddings: A foundation model for cell biology. *bioRxiv*, pages 2023–11, 2023. [2](#)

[42] Charlie Saillard, Rodolphe Jenatton, Felipe Llinares-López, Zelda Mariet, David Cahané, Eric Durand, and Jean-Philippe Vert. H-optimus-0, 2024. [2](#), [3](#)

[43] Anna C Schaar, Alejandro Tejada-Lapuerta, Giovanni Palla, Robert Gutgesell, Lennard Halle, Mariia Minaeva, Larsen Vornholz, Leander Dony, Francesca Drummer, Mojtaba Bahrami, et al. Nicheformer: a foundation model for single-cell and spatial omics. *bioRxiv*, pages 2024–04, 2024. [2](#), [4](#)

[44] Benoît Schmauch, Alberto Romagnoni, Elodie Pronier, Charlie Saillard, Pascale Maillé, Julien Calderaro, Aurélie Kamoun, Meriem Sefta, Sylvain Toldo, Mikhail Zaslavskiy, Thomas Clozel, Matahi Moarri, Pierre Courtiol, and Gilles

Wainrib. A deep learning model to predict RNA-seq expression of tumours from whole slide images. *Nat. Commun.*, 11(1):3877, 2020. 2

[45] George Shaikovski, Adam Casson, Kristen Severson, Eric Zimmermann, Yi Kan Wang, Jeremy D. Kunz, Juan A. Retamero, Gerard Oakley, David Klimstra, Christopher Kanan, Matthew Hanna, Michal Zelechowski, Julian Viret, Neil Tenenholz, James Hall, Nicolo Fusi, Razik Yousfi, Peter Hamilton, William A. Moye, Eugene Vorontsov, Siqi Liu, and Thomas J. Fuchs. Prism: A multi-modal generative foundation model for slide-level histopathology, 2024. 2

[46] Manuel Tran, Paul Schmidle, Sophia J Wagner, Valentin Koch, Valerio Lupperger, Annette Feuchtinger, Alexander Böhner, Robert Kaczmarczyk, Tilo Biedermann, Kilian Eyerich, et al. Generating highly accurate pathology reports from gigapixel whole slide images with histogpt. *medRxiv*, pages 2024–03, 2024. 1, 2

[47] Anurag Vaidya, Andrew Zhang, Guillaume Jaume, Andrew H Song, Tong Ding, Sophia J Wagner, Ming Y Lu, Paul Doucet, Harry Robertson, Cristina Almagro-Perez, et al. Molecular-driven foundation model for oncologic pathology. *arXiv preprint arXiv:2501.16652*, 2025. 1, 2

[48] Annika Vannan, Ruqian Lyu, Arianna L. Williams, Nicholas M. Negretti, Evan D. Mee, Joseph Hirsh, Samuel Hirsh, David S. Nichols, Carla L. Calvi, Chase J. Taylor, Vasiliy. V. Polosukhin, Ana PM Serezani, A. Scott McCall, Jason J. Gokey, Heejung Shim, Lorraine B. Ware, Matthew J. Bacchetta, Ciara M. Shaver, Timothy S. Blackwell, Rajat Walia, Jennifer MS Sucre, Jonathan A. Kropski, Davis J McCarthy, and Nicholas E. Banovich. Image-based spatial transcriptomics identifies molecular niche dysregulation associated with distal lung remodeling in pulmonary fibrosis. *bioRxiv*, 2023. 12

[49] Eugene Vorontsov, Alican Bozkurt, Adam Casson, George Shaikovski, Michal Zelechowski, Kristen Severson, Eric Zimmermann, James Hall, Neil Tenenholz, Nicolo Fusi, et al. A foundation model for clinical-grade computational pathology and rare cancers detection. *Nature medicine*, 30(10):2924–2935, 2024. 2

[50] Sophia J Wagner, Daniel Reisenbüchler, Nicholas P West, Jan Moritz Niehues, Jiefu Zhu, Sebastian Foersch, Gregory Patrick Veldhuizen, Philip Quirke, Heike I Grabsch, Piet A van den Brandt, et al. Transformer-based biomarker prediction from colorectal cancer histology: A large-scale multicentric study. *Cancer Cell*, 41(9):1650–1661, 2023. 2, 4, 15

[51] Chloe Xueqi Wang, Haotian Cui, Andrew Hanzhou Zhang, Ronald Xie, Hani Goodarzi, and Bo Wang. scgpt-spatial: Continual pretraining of single-cell foundation model for spatial transcriptomics. *bioRxiv*, pages 2025–02, 2025. 2

[52] Xiyue Wang, Sen Yang, Jun Zhang, Minghui Wang, Jing Zhang, Wei Yang, Junzhou Huang, and Xiao Han. Transformer-based unsupervised contrastive learning for histopathological image classification. *Medical image analysis*, 81:102559, 2022. 2, 3

[53] Xiyue Wang, Yuexi Du, Sen Yang, Jun Zhang, Minghui Wang, Jing Zhang, Wei Yang, Junzhou Huang, and Xiao Han. Retcl: Clustering-guided contrastive learning for whole-slide image retrieval. *Medical image analysis*, 83:102645, 2023. 2

[54] John N Weinstein, Eric A Collisson, Gordon B Mills, Kenna R Shaw, Brad A Ozenberger, Kyle Ellrott, Ilya Shmulevich, Chris Sander, and Joshua M Stuart. The cancer genome atlas pan-cancer analysis project. *Nature genetics*, 45(10):1113–1120, 2013. 4

[55] F Alexander Wolf, Philipp Angerer, and Fabian J Theis. SCANPY: large-scale single-cell gene expression data analysis. *Genome Biol.*, 19(1), 2018. 15

[56] Jinxi Xiang, Xiyue Wang, Xiaoming Zhang, Yinghua Xi, Feyisope Eweje, Yijiang Chen, Yuchen Li, Colin Bergstrom, Matthew Gopaulchan, Ted Kim, Kun-Hsing Yu, Sierra Willens, Francesca Maria Olguin, Jeffrey J. Nirschl, Joel Neal, Maximilian Diehn, Sen Yang, and Ruijiang Li. A vision-language foundation model for precision oncology. *Nature*, 638(8051):769–778, 2025. 2

[57] Ronald Xie, Kuan Pang, Sai Chung, Catia Perciani, Sonya MacParland, Bo Wang, and Gary Bader. Spatially resolved gene expression prediction from histology images via bi-modal contrastive learning. In *Advances in Neural Information Processing Systems*, pages 70626–70637. Curran Associates, Inc., 2023. 2, 8

[58] Hanwen Xu, Naoto Usuyama, Jaspreet Bagga, Sheng Zhang, Rajesh Rao, Tristan Naumann, Cliff Wong, Zelalem Gero, Javier González, Yu Gu, et al. A whole-slide foundation model for digital pathology from real-world data. *Nature*, 630(8015):181–188, 2024. 2, 3

[59] Xiaohua Zhai, Basil Mustafa, Alexander Kolesnikov, and Lucas Beyer. Sigmoid loss for language image pre-training, 2023. 4

[60] Andrew Zhang, Guillaume Jaume, Anurag Vaidya, Tong Ding, and Faisal Mahmood. Accelerating data processing and benchmarking of ai models for pathology, 2025. 2

[61] Daiwei Zhang, Amelia Schroeder, Hanying Yan, Haochen Yang, Jian Hu, Michelle Y Y Lee, Kyung S Cho, Katalin Susztak, George X Xu, Michael D Feldman, Edward B Lee, Emma E Furth, Linghua Wang, and Mingyao Li. Inferring super-resolution tissue architecture by integrating spatial transcriptomics with histology. *Nat. Biotechnol.*, pages 1–6, 2024. 2

[62] Yi Zheng, Regan D. Conrad, Emily J. Green, Eric J. Burks, Margrit Betke, Jennifer E. Beane, and Vijaya B. Kolachalam. Graph attention-based fusion of pathology images and gene expression for prediction of cancer survival. *IEEE Transactions on Medical Imaging*, 43(9):3085–3097, 2024. 2

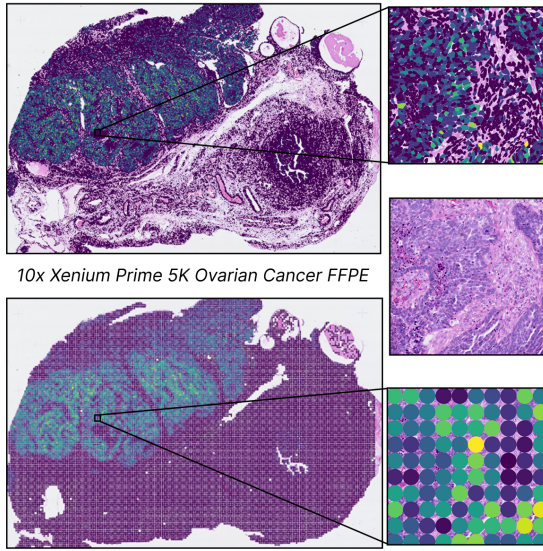


Figure 3. Top: Overlay of TP53 gene counts as observed in individual cells in Xenium Ovarian Cancer tissue. Bottom: Overlay of TP53 gene on simulated pseudo-bulk spot used to form the HES-CAPE dataset

7. Datasets

This section summarizes the spatial transcriptomics datasets used in this study. The datasets are organized by gene panel type. A summary table is provided in main Tab. 1. All tissue sections were imaged at 40x magnification and preserved using FFPE method (except where noted).

Since we use 10x Xenium samples with sub-cellular transcript detection, we need to simulate a 10x Visium patch of size $55\mu\text{m}$, called pseudo-spot, for patch-based image-gene pairs. We achieve this by sum pooling the transcripts of cells within the simulated spot. The aggregated gene expressions in the simulated spots follow similar distributions to the xenium gene expressions. This is additionally validated visually by plotting expression of several biomarker genes like TP53 on the spatial samples as seen in Fig. 3.

To enable efficient benchmarking, for each dataset above, we have also created an image patch–spatial expression dataset in the Hugging Face Arrow format, comprising a total of 7229962 image-gene expression pairs combined. Each pair is accompanied by patient-specific metadata and is available on the Hugging Face Hub. For the final benchmark, we filter out replicates with different gene panels and single gene panel datasets resulting in $\sim 620k$ image-gene expression pairs.

Patient-based stratification was employed for each dataset to create training, validation, and test splits ensuring that each patient’s samples are confined to a single split. Since a lot of 10x Xenium samples are part of the HEST-benchmark test set, for fair evaluation we design our own testing splits

and test all image models from HEST-benchmark on these new splits. All reported results are based on the provided test split to clearly expose the impact of batch effects.

All dataset preprocessing and creation was done using `SpatialData` [33] and `Huggingface Datasets` library

7.1. Detailed Description of Dataset Groups

7.1.1. Human 5K Panel

This panel contains 6 datasets spanning multiple organs including Skin, Prostate, Lymphoid, Lung, Breast, Cervix, and Ovary. All samples are from cancer or diseased tissue preserved with FFPE, except one Fresh Frozen ovarian cancer sample. The datasets have uniform pixel size around $0.274\ \mu\text{m}$.

7.1.2. Human Colon Panel

This panel includes 5 datasets exclusively focused on bowel tissue, with both cancerous and healthy samples. All samples are FFPE-preserved with pixel sizes ranging from $0.137\ \mu\text{m}$ to $0.274\ \mu\text{m}$. Three datasets come from the same study on immune cell populations in colorectal cancer, all from the same patient.

7.1.3. Human Lung Healthy Panel

The most extensive group with 19 datasets, all focused on lung tissue. Samples include both healthy (6 datasets) and diseased (13 datasets) states from 19 different patients with pulmonary fibrosis. All datasets are from the study Vannan et al. [48]. All images have consistent pixel size of $0.213\ \mu\text{m}$.

7.1.4. Human Immuno-Oncology Panel

This panel contains 5 datasets from 5 different organs (Ovary, Lung, Pancreas, Bowel, Brain), all studying cancerous tissue. Three datasets include identified patient information. All samples have consistent pixel size around $0.274\ \mu\text{m}$ and include custom add-ons to the base panel.

7.1.5. Human Multi-Tissue Panel

A diverse group of 14 datasets covering 8 different organs (Lymphoid, Bone, Pancreas, Skin, Liver, Heart, Lung, Kidney). Includes all three disease states (Cancer, Healthy, Diseased) with pixel sizes ranging from $0.137\ \mu\text{m}$ to $0.274\ \mu\text{m}$. Most datasets are organ-specific paired samples (cancer/healthy or diseased/healthy).

7.1.6. Human Breast Panel

Includes 5 datasets all focused on breast cancer tissue. Two datasets are from a study using the entire sample area from one patient, while three are from a high-resolution mapping study of tumor microenvironment. Pixel sizes range from $0.213\ \mu\text{m}$ to $0.364\ \mu\text{m}$.

Table 7. Complete Test Recall@1 Results for both Image-to-Gene (I2G) and Gene-to-Image (G2I) tasks across different tissue panels. Experiments with “—” indicate out of memory issues during training

Model	5K		Multi		ImmOnc		Colon		Breast		Lung	
	I2G	G2I										
MLP-CTransPath	0.022(0.002)	0.023(0.004)	0.029(0.004)	0.020(0.003)	0.023(0.002)	0.019(0.003)	0.020(0.004)	0.026(0.008)	0.026(0.005)	0.025(0.002)	0.022(0.004)	0.028(0.004)
MLP-CONCH	0.058(0.007)	0.058(0.006)	0.056(0.005)	0.041(0.005)	0.044(0.004)	0.028(0.002)	0.074(0.009)	0.062(0.005)	0.106(0.019)	0.067(0.011)	0.134(0.007)	0.127(0.013)
MLP-Gigapath	0.069(0.006)	0.067(0.002)	0.074(0.006)	0.051(0.005)	0.042(0.002)	0.028(0.002)	0.077(0.012)	0.073(0.010)	0.091(0.015)	0.079(0.007)	0.173(0.001)	0.165(0.005)
MLP-H0mini	0.059(0.002)	0.060(0.001)	0.048(0.009)	0.033(0.004)	0.041(0.005)	0.027(0.001)	0.071(0.006)	0.072(0.012)	0.086(0.005)	0.060(0.004)	0.099(0.005)	0.093(0.006)
MLP-UNI	0.065(0.011)	0.064(0.009)	0.061(0.006)	0.039(0.006)	0.060(0.009)	0.029(0.006)	0.079(0.001)	0.080(0.007)	0.091(0.015)	0.065(0.014)	0.164(0.016)	0.164(0.019)
scFoundation-CTransPath	—	—	—	—	0.024(0.002)	0.028(0.003)	0.022(0.002)	0.019(0.005)	0.028(0.002)	0.026(0.004)	0.029(0.002)	0.028(0.002)
scFoundation-CONCH	—	—	—	—	0.055(0.006)	0.043(0.003)	0.077(0.008)	0.068(0.011)	0.085(0.012)	0.082(0.016)	0.166(0.005)	0.147(0.014)
scFoundation-Gigapath	—	—	—	—	0.065(0.007)	0.052(0.009)	0.079(0.013)	0.064(0.004)	0.090(0.005)	0.102(0.015)	0.225(0.022)	0.195(0.027)
scFoundation-H0mini	—	—	—	—	0.050(0.003)	0.042(0.005)	0.080(0.007)	0.067(0.005)	0.112(0.006)	0.104(0.011)	0.131(0.011)	0.094(0.005)
scFoundation-UNI	—	—	—	—	0.058(0.005)	0.040(0.004)	0.079(0.008)	0.060(0.021)	0.094(0.008)	0.094(0.015)	0.191(0.011)	0.158(0.011)
Nicheformer-CTransPath	0.023(0.001)	0.024(0.001)	0.027(0.003)	0.024(0.002)	0.027(0.001)	0.027(0.001)	0.018(0.003)	0.021(0.004)	0.025(0.004)	0.027(0.003)	0.027(0.004)	0.031(0.003)
Nicheformer-CONCH	0.061(0.001)	0.076(0.006)	0.067(0.005)	0.077(0.003)	0.056(0.003)	0.063(0.004)	0.069(0.006)	0.068(0.003)	0.101(0.008)	0.123(0.004)	0.125(0.002)	0.164(0.003)
Nicheformer-Gigapath	0.062(0.002)	0.067(0.001)	0.075(0.007)	0.079(0.005)	0.063(0.004)	0.072(0.005)	0.067(0.005)	0.073(0.006)	0.121(0.008)	0.139(0.016)	0.155(0.006)	0.203(0.005)
Nicheformer-H0mini	0.065(0.004)	0.076(0.001)	0.069(0.006)	0.077(0.008)	0.053(0.002)	0.054(0.002)	0.076(0.007)	0.075(0.009)	0.125(0.011)	0.142(0.003)	0.129(0.007)	0.168(0.013)
Nicheformer-UNI	0.071(0.006)	0.082(0.003)	0.073(0.002)	0.079(0.002)	0.060(0.008)	0.067(0.007)	0.063(0.002)	0.066(0.004)	0.122(0.013)	0.136(0.004)	0.144(0.003)	0.188(0.006)
DRV1-CTransPath	0.023(0.000)	0.025(0.001)	0.026(0.001)	0.033(0.002)	0.031(0.003)	0.028(0.003)	0.022(0.004)	0.026(0.004)	0.036(0.004)	0.032(0.006)	0.032(0.004)	0.037(0.003)
DRV1-CONCH	0.073(0.005)	0.093(0.002)	0.084(0.000)	0.110(0.004)	0.083(0.005)	0.081(0.002)	0.098(0.010)	0.108(0.010)	0.117(0.022)	0.124(0.011)	0.195(0.004)	0.240(0.002)
DRV1-Gigapath	0.097(0.011)	0.115(0.003)	0.097(0.005)	0.134(0.007)	0.103(0.004)	0.101(0.005)	0.111(0.008)	0.121(0.010)	0.146(0.010)	0.142(0.008)	0.283(0.002)	0.329(0.006)
DRV1-H0mini	0.085(0.005)	0.096(0.003)	0.077(0.008)	0.100(0.009)	0.079(0.006)	0.072(0.004)	0.123(0.001)	0.126(0.004)	0.147(0.010)	0.152(0.009)	0.208(0.001)	0.249(0.002)
DRV1-UNI	0.097(0.002)	0.106(0.007)	0.092(0.007)	0.126(0.005)	0.094(0.007)	0.090(0.003)	0.122(0.004)	0.124(0.004)	0.142(0.023)	0.145(0.021)	0.242(0.009)	0.301(0.014)

Table 8. Complete Test Recall@10 Results for both Image-to-Gene (I2G) and Gene-to-Image (G2I) tasks across different tissue panels. Experiments with “—” indicate out of memory issues during training

Model	5K		Multi		ImmOnc		Colon		Breast		Lung	
	I2G	G2I										
MLP-CTransPath	0.194(0.008)	0.203(0.017)	0.265(0.015)	0.191(0.011)	0.215(0.015)	0.183(0.008)	0.197(0.028)	0.235(0.081)	0.220(0.033)	0.2200(0.016)	0.196(0.014)	0.234(0.039)
MLP-CONCH	0.388(0.050)	0.387(0.041)	0.414(0.027)	0.314(0.021)	0.333(0.013)	0.241(0.009)	0.501(0.040)	0.440(0.010)	0.586(0.060)	0.421(0.038)	0.642(0.024)	0.605(0.036)
MLP-Gigapath	0.420(0.021)	0.425(0.015)	0.495(0.024)	0.371(0.019)	0.321(0.015)	0.244(0.008)	0.528(0.036)	0.500(0.028)	0.595(0.049)	0.441(0.036)	0.693(0.020)	0.675(0.016)
MLP-H0mini	0.401(0.009)	0.399(0.008)	0.371(0.047)	0.279(0.029)	0.313(0.020)	0.224(0.013)	0.502(0.047)	0.492(0.058)	0.486(0.018)	0.384(0.017)	0.552(0.006)	0.523(0.003)
MLP-UNI	0.409(0.036)	0.409(0.036)	0.435(0.028)	0.306(0.032)	0.412(0.034)	0.243(0.031)	0.532(0.008)	0.524(0.035)	0.545(0.027)	0.403(0.047)	0.684(0.040)	0.677(0.061)
scFoundation-CTransPath	—	—	—	—	0.224(0.013)	0.232(0.017)	0.204(0.036)	0.192(0.037)	0.254(0.011)	0.2360(0.020)	0.230(0.008)	0.225(0.017)
scFoundation-CONCH	—	—	—	—	0.373(0.021)	0.314(0.015)	0.473(0.049)	0.439(0.039)	0.517(0.035)	0.497(0.051)	0.691(0.010)	0.656(0.024)
scFoundation-Gigapath	—	—	—	—	0.416(0.028)	0.352(0.029)	0.473(0.075)	0.422(0.014)	0.554(0.004)	0.567(0.030)	0.768(0.024)	0.733(0.043)
scFoundation-H0mini	—	—	—	—	0.358(0.013)	0.304(0.033)	0.513(0.004)	0.455(0.037)	0.581(0.021)	0.578(0.036)	0.616(0.019)	0.536(0.015)
scFoundation-UNI	—	—	—	—	0.398(0.023)	0.312(0.014)	0.482(0.029)	0.413(0.095)	0.557(0.018)	0.552(0.051)	0.726(0.009)	0.670(0.029)
Nicheformer-CTransPath	0.202(0.007)	0.218(0.005)	0.237(0.021)	0.224(0.030)	0.241(0.010)	0.233(0.011)	0.179(0.022)	0.212(0.026)	0.207(0.023)	0.242(0.018)	0.228(0.027)	0.256(0.030)
Nicheformer-CONCH	0.395(0.008)	0.443(0.023)	0.422(0.010)	0.459(0.006)	0.375(0.009)	0.410(0.013)	0.444(0.029)	0.409(0.022)	0.569(0.016)	0.612(0.010)	0.609(0.001)	0.692(0.011)
Nicheformer-Gigapath	0.395(0.011)	0.417(0.011)	0.441(0.021)	0.458(0.017)	0.405(0.021)	0.434(0.006)	0.433(0.016)	0.439(0.038)	0.621(0.019)	0.648(0.027)	0.667(0.011)	0.742(0.006)
Nicheformer-H0mini	0.396(0.014)	0.439(0.009)	0.430(0.023)	0.448(0.023)	0.355(0.009)	0.356(0.007)	0.470(0.038)	0.450(0.042)	0.620(0.018)	0.649(0.018)	0.617(0.013)	0.696(0.022)
Nicheformer-UNI	0.422(0.020)	0.466(0.009)	0.436(0.006)	0.462(0.005)	0.406(0.033)	0.427(0.033)	0.423(0.021)	0.402(0.019)	0.623(0.033)	0.639(0.003)	0.644(0.004)	0.726(0.005)
DRV1-CTransPath	0.204(0.006)	0.215(0.008)	0.222(0.013)	0.272(0.012)	0.258(0.015)	0.246(0.014)	0.212(0.025)	0.226(0.033)	0.289(0.015)	0.273(0.030)	0.264(0.017)	0.292(0.018)
DRV1-CONCH	0.431(0.020)	0.488(0.011)	0.471(0.004)	0.549(0.013)	0.471(0.011)	0.463(0.020)	0.561(0.034)	0.556(0.040)	0.591(0.050)	0.591(0.031)	0.714(0.011)	0.764(0.003)
DRV1-Gigapath	0.479(0.041)	0.534(0.013)	0.499(0.018)	0.607(0.015)	0.519(0.019)	0.508(0.014)	0.594(0.011)	0.597(0.028)	0.660(0.024)	0.626(0.027)	0.800(0.001)	0.849(0.003)
DRV1-H0mini	0.468(0.012)	0.495(0.010)	0.434(0.022)	0.523(0.018)	0.450(0.014)	0.431(0.015)	0.617(0.012)	0.590(0.019)	0.664(0.023)	0.661(0.023)	0.739(0.001)	0.778(0.004)
DRV1-UNI	0.496(0.011)	0.521(0.023)	0.486(0.023)	0.579(0.026)	0.503(0.022)	0.500(0.008)	0.611(0.021)	0.600(0.013)	0.648(0.050)	0.629(0.045)	0.772(0.002)	0.826(0.008)

7.2. Additional datasets

We also include 4 datasets studying breast cancer tissue from two patients in the HESCAPE dataset. These datasets were not used for any experiments above, but are can be useful for further downstream tasks. Each patient has two datasets: one with a custom add-on panel and one with a pre-designed panel, allowing for direct comparison. All datasets have consistent pixel size of 0.213 μm .

7.2.1. Preservation Methods

Only one dataset, Xenium_Prime_Human_Ovary_FF, uses Fresh Frozen preservation for ovarian cancer tissue.

7.2.2. Imaging Parameters

All datasets were imaged at 40x magnification. Pixel sizes range from 0.137 μm to 0.364 μm , with most datasets having pixel sizes around 0.213 μm or 0.274 μm .

8. Pretraining

8.1. Implementation details

For consistency, both encoders output embeddings of dimension $d = 128$. The training is performed with gradient clipping set to 5.0, a batch size of 256 distributed across 4 GPUs for 20,000 steps, and an initial warmup phase of 780 steps. We use an AdamW optimizer β : (0.9, 0.95) with a learning rate starting at 1×10^{-5} reduced over iterations via a cosine scheduler, and a weight decay of 0.01. The full contrastive pretraining is performed with a finetuning image-tuning and locked gene encoding objective, allowing the image encoders to learn robust, gene-biomarker specific features. All experiments are conducted on a Slurm GPU cluster equipped with A100 GPUs. We use PyTorch and Hydra for all our experiments.

Table 9. Projection head ablation study: Experiments performed with CLIP loss and frozen encoders. Best results are in **bold**, second-best are underlined.

Model	projection	5K		Colon	
		I2G	G2I	I2G	G2I
DRV1-Gigapath	linear	0.170	0.180	<u>0.295</u>	0.274
DRV1-UNI	linear	0.172	0.180	<u>0.243</u>	0.251
DRV1-Gigapath	mlp	0.201	0.210	0.317	0.328
DRV1-UNI	mlp	0.201	<u>0.201</u>	0.289	0.231
DRV1-Gigapath	transformer	0.114	0.130	0.250	<u>0.277</u>
DRV1-UNI	transformer	0.135	0.166	0.179	0.245

Table 10. Loss function ablation study: Experiments performed with same configuration as the benchmark. Best results are in **bold**, second-best are underlined.

Model	loss	5K		Colon	
		I2G	G2I	I2G	G2I
DRV1-Gigapath	CLIP	<u>0.315</u>	0.359	<u>0.388</u>	0.394
DRV1-UNI	CLIP	0.322	0.341	0.404	0.401
DRV1-Gigapath	SIGLIP	0.322	<u>0.352</u>	0.377	0.345
DRV1-UNI	SIGLIP	0.292	0.293	0.359	0.359

Table 11. Encoder Finetuning ablation study: Experiments performed with CLIP loss and MLP projection head. Experiments with "—" indicate out of memory issues during training. Best results are in **bold**, second-best are underlined.

Model	finetune		5K		Colon	
	img	gene	I2G	G2I	I2G	G2I
Nicheformer-UNI	✗	✗	0.153	0.174	0.201	0.221
Nicheformer-Gigapath	✗	✗	0.149	0.169	0.195	0.221
DRV1-UNI	✗	✗	0.172	0.180	0.243	0.251
DRV1-Gigapath	✗	✗	0.170	0.180	0.295	0.274
Nicheformer-UNI	✗	✓	0.187	0.205	0.261	0.266
Nicheformer-Gigapath	✗	✓	0.188	0.197	0.282	0.292
DRV1-UNI	✗	✓	0.204	0.225	0.318	0.319
DRV1-Gigapath	✗	✓	0.198	0.208	0.311	0.343
Nicheformer-UNI	✓	✗	0.262	0.282	0.238	0.244
Nicheformer-Gigapath	✓	✗	0.277	0.296	0.249	0.266
DRV1-UNI	✓	✗	0.289	0.293	0.326	0.284
DRV1-Gigapath	✓	✗	0.269	0.335	0.333	<u>0.362</u>
Nicheformer-UNI	✓	✓	<u>0.308</u>	0.317	0.323	0.326
Nicheformer-Gigapath	✓	✓	—	—	—	—
DRV1-UNI	✓	✓	0.358	<u>0.342</u>	0.335	0.336
DRV1-Gigapath	✓	✓	0.299	0.370	<u>0.334</u>	0.376

8.2. Ablation study

To measure the contributing factors of different hyperparameters and architectural changes towards contrastive alignment performance, we performed 3 independent ablation studies. The ablations were performed on the pan-organ 5K gene panel and the Colon panel.

8.2.1. Image Projection head

The ablation was to see which of the 3 heads, the basic linear projection, MLP or a transformer based projection helps improve the image encodings during contrastive pretraining. The results in Tab. 9 show, that MLP as an image projection head performs consistently well across both datasets.

8.2.2. Loss function

Here, we test both CLIP and SigLip losses across the 5K and Colon pretraining experiments to understand their performance in our data and batch size configurations. Our ablations in Tab. 10 suggests, there was no substantial improvement from using SigLip as the loss function.

The SigLip loss for the image-gene expression pair v_{2g} is:

$$L_{\text{SIGLIP}^{v_{2g}}} = -\frac{1}{|\mathcal{B}|} \sum_{i=1}^{|\mathcal{B}|} \sum_{j=1}^{|\mathcal{B}|} \log \frac{1}{1 + \exp[z_{ij}(-\tau \langle \mathbf{v}_i, \mathbf{g}_j \rangle + b)]} \quad (3)$$

with an additional learnable bias b . Unlike CLIP loss, SIGLIP avoids computing a global normalization and instead formalizes the objective as a logistic regression task, where the label z_{ij} is 1 for the positive pair and is -1 for all the other pairs.

8.2.3. Encoder Finetuning

In the contrastive pretraining stage, HESCAPE is capable of performing both full fine-tuning for small models and parameter-efficient fine tuning (PEFT) for large transformer-based models. These approaches help to align the pretrained models to the other modality, while potentially helping the encoders to adapt to specific tasks and potentially mitigating problems arising from batch effects.

To evaluate whether frozen pretrained encoders alone are sufficient for multimodal image-gene alignment, we conducted ablation experiments using various combinations of image-gene finetuning. We fine-tune the self-attention query-key-value embeddings and projection layers of the image encoder using LoRA [16]. In our ablation study, we find that both unlocked image and gene models enable better image-gene alignment when possible Tab. 11. However, we can often be restricted by the compute resources for large multimodal Foundation Model finetuning. Additionally, since the gene modality is deeply affected by batch effects, we decided to keep the gene models frozen for the HESCAPE benchmark.

8.3. Batch effects on gene expression modality

During dataset curation and preprocessing, we observed strong batch effects across samples of the same tissue type in all datasets under consideration. To systematically investigate how these batch effects impact contrastive pretraining performance, we employed the silhouette-batch metric from the single-cell integration benchmark scib [31].

We computed this metric for all datasets using Leiden clustering results after standard scanpy preprocessing [55] as the *label key*, and the train-validation-test split as the *batch key*. By treating the dataset split as batch information, we quantified how well integrated the gene expression profiles are across different data splits, a measure that reflects the presence of technical artifacts in the gene expression modality.

Fig. 2 shows the relationship between silhouette-batch values and average Recall@5 performance for the Gigapath-DRVI model across all datasets. Notably, we observe a clear linear relationship between retrieval performance and the batch integration metric, directly supporting our hypothesis that batch effects significantly impact contrastive pretraining effectiveness. Specifically, our analysis confirms that cancer tissues exhibit significant heterogeneity in cellular composition and transcriptomic profiles relative to healthy or non-cancerous diseased samples. Our findings reveal pronounced batch effects in cancer samples as seen in the organ specific datasets, especially in breast and colon tissues, whereas lung samples with homogeneous disease conditions, in particular, patients with pulmonary fibrosis, show minimal batch variation. Technical variability can further exacerbating these differences - 10x Visium samples, for instance, are particularly prone to batch effects compared to Xenium.

8.4. Downstream task: gene mutation prediction

For the evaluation of gene mutation prediction, we use a weakly-supervised learning approach for predicting the slide-level mutation targets from frozen patch-level embeddings of the pretrained models.

For feature extraction, we use the pipeline TRIDENT¹ with default parameters, extracting embeddings from patches of size 256×256 pixels at $20 \times$ magnification. The pretrained HESCAPE models have a latent dimension of 128.

For slide-level mutation prediction, we follow the Histo-Bistro pipeline². Concretely, we employ Transformer-based feature aggregation using a two-layer Transformer architecture with eight heads of dimension 64 and latent dimension 512 [50]. We split the TCGA cohorts into five site-preserving folds for five-fold cross validation, using three folds for training, one for validation, and one for testing. We train the models for 10 epochs using the optimizer AdamW with learning rate of 2×10^{-5} , weight decay of 2×10^{-5} , and batch size 1. The best model is chosen based on the validation loss, evaluated every 500 iterations.

¹<https://github.com/mahmoodlab/TRIDENT>

²<https://github.com/peng-lab/HistoBistro>